Delft University of Technology

Spatial and temporal reconstruction of unsteady rotating forces through an inverse acoustic method

Xu, Ying; Zhang, Xiao Zheng; Casalino, Damiano; Bi, Chuan Xing

Citation (APA)
Xu, Y., Zhang, X. Z., Casalino, D., & Bi, C. X. (2023). Spatial and temporal reconstruction of unsteady rotating forces through an inverse acoustic method. *Mechanical Systems and Signal Processing*, *200*, Article 110596. https://doi.org/10.1016/j.ymssp.2023.110596

Important note
To cite this publication, please use the final published version (if applicable).
Please check the document version above.

Spatial and temporal reconstruction of unsteady rotating forces through an inverse acoustic method

Ying Xu [a], Xiao-Zheng Zhang [a], Damiano Casalino [b], Chuan-Xing Bi [a],[*]

[a] *Institute of Sound and Vibration Research, Hefei University of Technology, 193 Tunxi Road, Hefei 230009, People's Republic of China*
[b] *Flow Physics and Technology Department, Delft University of Technology, Kluyverweg 1, 2629HS Delft, The Netherlands*

A R T I C L E   I N F O

A B S T R A C T

An inverse acoustic method is presented in this work, which allows to determine the spatial and temporal distribution of unsteady rotating forces from microphone array measurements. The method is based on the usage of a space–time regularization with a mixed norm. The proposed method can take advantage of a prior knowledge of the space–time characteristics of the unsteady rotating forces to ensure an accurate force reconstruction in real-time, using a smaller number of input signals compared to more conventional inverse methods. Different properties of the proposed method are initially investigated by using synthetic acoustic signals radiated from rotating point sources and computed via an acoustic analogy formulation. Finally, the method is validated by using experimental acoustic signals radiated from the rotor of an unmanned aerial vehicle.

1. Introduction

The real-time spatial and temporal reconstruction of unsteady rotating forces is of paramount importance for the identification and control of noise generation mechanisms in rotating machines, such as propellers, rotors, turbofans and wind-turbines. The theory of sound generation from rotating forces is fully established since the pioneering publication of the generalized acoustic analogy formulation by Ffowcs-Williams and Hawkings in 1969 [1] and subsequent mathematical declinations of the theory seeded by Farassat [2–5]. These formulations allow computing the noise generated by rotating forces arbitrarily varying in space and time and are routinely applied in several industrial fields [6–11].

The experimental identification of spatial–temporal noise source distributions is usually carried out using pressure signals simultaneously acquired by microphones distributed on an array [12–15]. The most popular identification methods based on microphone array measurements fall into two main categories: the beamforming methods [16–18], and the inverse methods [19,20]. The main conceptual difference between these methods is that the beamforming methods are exhaustive search techniques where a selected grid containing the location of potential sound sources is scanned, while the inverse methods aim at solving an inverse problem accounting for the presence of all sound sources at once [15]. As discussed hereafter, only few attempts have been accomplished so far to use the theory of noise from rotating forces to identify loading-noise source distributions from microphone array measurements.

The beamforming methods are widely used in aeroacoustics, in virtue of their flexible measurement procedure and high computational efficiency. However, most of these beamforming methods are based on either static dipole sources [21–27] or moving

---

monopole sources [28–31] and have been rarely used for the identification of rotating loading sources. Recently, Pan et al., [32] developed a beamforming correction method in the frequency domain to identify rotating loading sources. Chen et al., [33] proposed a beamforming method in the time–frequency domain based on a moving dipole source formulation and obtained acoustic imaging results at different frequencies from an array located on the side of a propeller. However, a significant drawback of the beamforming methods is that it fails to quantify the source strengths accurately when multiple coherent sources are present.

The inverse methods have been used for the localization and quantification of unsteady rotating loading sources. Li *et al.*, [34,35] proposed an inverse method based on the Farassat integral solution of the the Ffowcs-Williams and Hawkings (FW-H) equation to reconstruct the steady aerodynamic forces acting on the surface of a propeller blade, which is responsible of the so-called rotor-locked noise contribution. Gerard *et al.,* [36,37] investigated an inverse method based on the Helmholtz integral solution following the approach of Morse and Ingard to evaluate the unsteady rotating forces acting by the fan on the fluid. Trabelsi *et al.,* [38] also developed an inverse method to evaluate the unsteady rotating forces acting on the fluid by the fan, but they employed a simple model of the tonal noise of an axial flow fan, in which the distributed force was replaced by an equivalent force concentrated at the aerodynamic center of the blade.

In the above-mentioned researches based on inverse methods, the reconstruction of the unsteady rotating forces was carried out in the frequency domain, thus losing some information about the variation of the sources in time. However, the capability to identify sources in space and time is key for real-time identification and control of rotating loading noise sources. Previous researches based on the time domain inverse method usually assume that the sources are simple monopole sources in stationary or rotating states [39–42]. Recently, Bi et al., [43] proposed a time-domain inverse method based on a conventional least-square regularization, hereinafter referred to as C-TDIM, to reconstruct the time histories of the three components of the unsteady rotating forces in the Cartesian co-ordinate system. However, a large number of spatial sampling points are required by that method to ensure a sufficiently accurate reconstruction of the unsteady rotating forces, which is due to the least-square approach used to invert the acoustic problem. In addition, the conventional regularization methods commonly used to solve force reconstruction problems in time domain, such as Tikhonov-based methods [44–48] and Least Absolute Shirinkage and Selection Operator (LASSO) regularization methods [49–53], cannot be well adapted to tackle both spatial localization and temporal reconstruction problems, simultaneously, since they are generally restricted to the reconstruction of force signals with the same space and time characteristics. In order to alleviate this limitation, this work proposes a time-domain inverse method based on a space–time regularization with a mixed norm, hereinafter referred to as ST-TDIM, to perform both spatial and temporal reconstruction of unsteady rotating forces. It should be pointed out that this method should overcome the intrinsic difficulty related to the different nature of spatial and temporal distributions: loading noise sources in rotating machines that operate in nominal conditions are typically continuous and regular in time, and concentrated in space in the blade tip region. The proposed method can take advantage of a prior knowledge of the space–time characteristics of the unsteady rotating forces to accurately and efficiently reconstruct them, in real-time, by reducing the required spatial resolution of the input noise measurements.

The remainder of the present paper is organized as follows. Section 2 presents the theoretical formulation of the proposed method. In Sec. 3, synthetic noise signals radiated by two unsteady rotating point forces are computed analytically and used as an input of the proposed method to systematically evaluate its accuracy and computational performance. In Sec. 4, experimental noise signals emitted by an unmanned aerial vehicle (UAV) rotor are used to validate the method in a more realistic operational scenario. Finally, the main outcome and conclusions of the present work are drawn in Sec. 5.
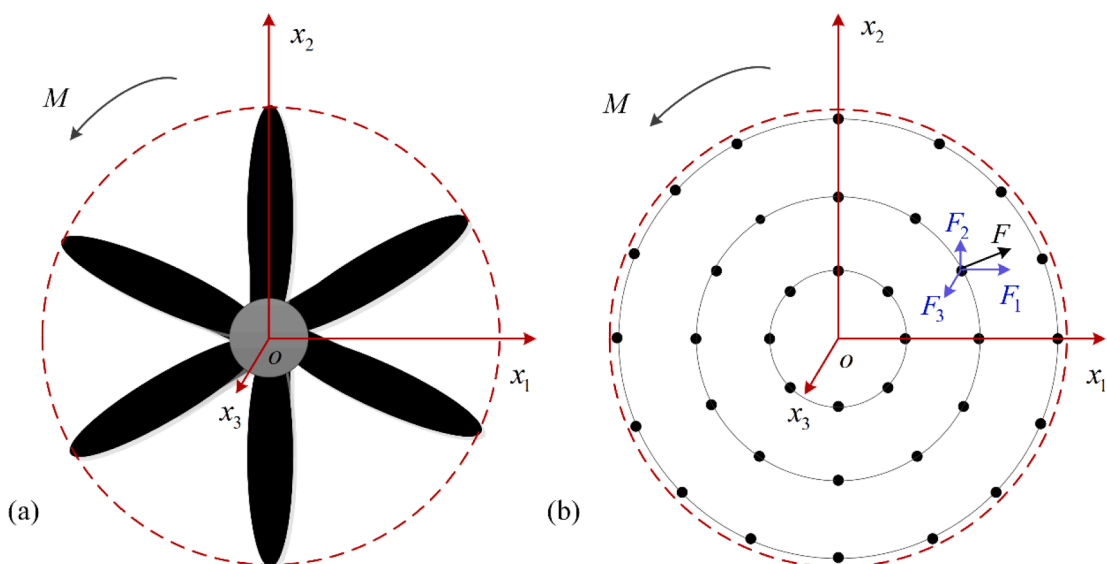

Fig. 1. Geometric description of the fan blade planform (a) and the source point distribution (b). The circular area drawn by dashed line represents the rotor disk. Solid circles identify locations of the point forces.

2. Theoretical formulations

2.1. The time-domain inversion procedure

Following the aeroacoustic theories based on Lighthill's acoustic analogy extended to bodies in arbitrary motion, a surface pressure distribution on a blade, which is steady (constant) or unsteady (time varying) in the blade reference system, act as a distribution of dipolar sources with strength proportional to pressure and its time derivative, respectively [1–5]. This noise generation mechanism is referred to as loading noise. For thin-blade rotors operating at subsonic tip velocity conditions (tip speeds with Mach numbers under 0.7), the loading noise contribution dominates over other contributions due to the fluid displacement caused by the blade motion (thickness noise) and to non-linear effects related to turbulence and/or shocks around the blades (quadrupole noise) [54].

By assuming chord-wise acoustic compactness (acoustic wavelength much larger than the blade chord), the planform of thin blades can be discretized into N point forces located along the blade span and at different azimuth in the rotor disk [54,55]. The source locations are marked by solid circles in Fig. 1, the force at each source point is decomposed into three components in the Cartesian coordinate system. The derivations start from the equations of sound pressure at a given microphone location x and time t generated by these N loading sources. By using the retarded time formulation 1A by Farassat [56], the pressure signal reads:

$$p(\boldsymbol{x},t) = \frac{1}{4\pi c} \sum_{n=1}^{N} \left[\frac{R_{ni}\dot{F}_{ni}}{R_n^2 \left(1 - M_{ni}\widetilde{R}_{ni}\right)^2} \right]_e - \frac{1}{4\pi} \sum_{n=1}^{N} \left[\frac{M_{ni}F_{ni}}{R_n^2 \left(1 - M_{ni}\widetilde{R}_{ni}\right)^2} \right]_e$$
$$+ \frac{1}{4\pi c} \sum_{n=1}^{N} \left[\frac{\left(R_{ni}\dot{M}_{ni}\right)R_{ni}F_{ni}}{R_n^3 \left(1 - M_{ni}\widetilde{R}_{ni}\right)^3} \right]_e + \frac{1}{4\pi} \sum_{n=1}^{N} \left[\frac{\left(1 - M_n^2\right)R_{ni}F_{ni}}{R_n^3 \left(1 - M_{ni}\widetilde{R}_{ni}\right)^3} \right]_e \tag{1}$$

where the subscript ''n'' indicates the nth source point; $\dot{F}_{ni}$ is the derivative of the force component of the nth source F_{ni} with respect to the source time, i.e., $\dot{F}_{ni} = \partial F_{ni}/\partial\tau$; R_{ni} is the component of the distance vector from the nth source to the observer; R_n is the amplitude of the distance vector; $\widetilde{R}_{ni}$ is the derivative of R_{ni} with respect to space, i.e., $\widetilde{R}_{ni} = \partial R_n/\partial x_i$; M_{ni} is the Mach number component of the nth source, with $M_{ni} = V_{ni}/c$ where V_{ni} is the velocity component of the nth source; M_n is the Mach number of the nth source; $\dot{M}_{ni}$ is the derivative of M_{ni} in terms of the source time, i.e., $\dot{M}_{ni} = \partial M_{ni}/\partial\tau$. The subscript ''$e$'' in Eq. (1) indicates that all the quantities in the square brackets depend on their evaluated values at the retarded source time τ.

The observation and source time are also discretized. Thus the sampling observer time steps t^k and the source time steps τ^l are defined as:

$$t^k = t^1 + (k-1)\Delta t, \quad k = 1, 2, \ldots, K \tag{2}$$

$$\tau^l = \tau^1 + (l-1)\Delta t, \quad l = 1, 2, \ldots, L \tag{3}$$

When using the discrete pressure values to calculate the force values, the source time for each loading source should be determined first as:

$$\tau_n^k = t^k - R_n/c \tag{4}$$

Due to Doppler effects, the source time τ_n^k will not be an integer multiple of the given time interval Δt. Therefore, the force component should be processed by the following time domain interpolation:

$$F_{ni}\left(\tau_n^k\right) = \sum_{l=1}^{k} \zeta^l\left(\tau_n^k\right) F_{ni}^l \tag{5}$$

$$\dot{F}_{ni}\left(\tau_n^k\right) = \sum_{l=1}^{k} \frac{\partial \zeta^l\left(\tau_n^k\right)}{\partial\tau} F_{ni}^l \tag{6}$$

where F_{ni}^l represents the force component at each source time step τ^l; $\zeta^l(\tau_n^k)$ is the Lagrange linear interpolation function [41,42].

After the discretization and interpolation, Eq. (1) becomes

$$p(\boldsymbol{x}, t^k) = \sum_{n=1}^{N} \sum_{l=1}^{k} g_{ni}^l\left(\tau_n^k\right) F_{ni}^l \tag{7}$$

where $g_{ni}^l(\tau_n^k)$ is expressed as:

$$g_{ni}^l(\tau_n^k) = \frac{R_{ni}}{4\pi c R_n^2\left(1-M_{ni}\widetilde{R}_{ni}\right)^2}\frac{\partial\zeta^l(\tau_n^k)}{\partial\tau} - \frac{M_{ni}}{4\pi R_n^2\left(1-M_{ni}\widetilde{R}_{ni}\right)^2}\zeta^l(\tau_n^k)$$

$$+ \frac{\left(R_{ni}\dot{M}_{ni}\right)R_{ni}}{4\pi c R_n^3\left(1-M_{ni}\widetilde{R}_{ni}\right)^3}\zeta^l(\tau_n^k) + \frac{\left(1-M_n^2\right)R_{ni}}{4\pi R_n^3\left(1-M_{ni}\widetilde{R}_{ni}\right)^3}\zeta^l(\tau_n^k) \tag{8}$$

In a matrix form, Eq. (7) can be rewritten as:

$$p(\boldsymbol{x}, t^k) = \boldsymbol{\psi}^{1k}\boldsymbol{T}^1 + \boldsymbol{\psi}^{2k}\boldsymbol{T}^2 + \cdots + \boldsymbol{\psi}^{lk}\boldsymbol{T}^l + \cdots + \boldsymbol{\psi}^{kk}\boldsymbol{T}^k \tag{9}$$

where

$$\boldsymbol{\psi}^{lk} = [\, g_{11}^l(\tau_1^k) \quad \cdots \quad g_{N1}^l(\tau_N^k) \quad g_{12}^l(\tau_1^k) \quad \cdots$$
$$g_{N2}^l(\tau_N^k) \quad g_{13}^l(\tau_1^k) \quad \cdots \quad g_{N3}^l(\tau_N^k)\,] \tag{10}$$

$$\boldsymbol{T}^l = \begin{bmatrix} F_{11}^l & \cdots & F_{N1}^l & F_{12}^l & \cdots & F_{N2}^l & F_{13}^l & \cdots & F_{N3}^l \end{bmatrix}^{\mathrm{T}} \tag{11}$$

By considering Q measurement points (microphones), and by applying Eq. (9) to each measurement point, yields the following extended matrix equation:

$$\boldsymbol{P}^k = \boldsymbol{H}^{1k}\boldsymbol{T}^1 + \boldsymbol{H}^{2k}\boldsymbol{T}^2 + \cdots + \boldsymbol{H}^{lk}\boldsymbol{T}^l + \cdots + \boldsymbol{H}^{kk}\boldsymbol{T}^k \tag{12}$$

where

$$\boldsymbol{P}^k = \begin{bmatrix} p(\boldsymbol{x}_1, t^k) & p(\boldsymbol{x}_2, t^k) & \cdots & p(\boldsymbol{x}_q, t^k) & \cdots & p(\boldsymbol{x}_Q, t^k) \end{bmatrix}^{\mathrm{T}} \tag{13}$$

$$\boldsymbol{H}^{lk} = \begin{bmatrix} \left(\boldsymbol{\psi}_1^{lk}\right)^{\mathrm{T}} & \left(\boldsymbol{\psi}_2^{lk}\right)^{\mathrm{T}} & \cdots & \left(\boldsymbol{\psi}_q^{lk}\right)^{\mathrm{T}} & \cdots & \left(\boldsymbol{\psi}_Q^{lk}\right)^{\mathrm{T}} \end{bmatrix}^{\mathrm{T}} \tag{14}$$

By applying Eq. (12) to each time step, the problem can be casted in a large matrix form, i.e.:

$$\boldsymbol{P} = \overleftrightarrow{\boldsymbol{H}}\ \overleftrightarrow{\boldsymbol{T}} \tag{15}$$

where

$$\boldsymbol{P} = \begin{bmatrix} \boldsymbol{P}^1 & \boldsymbol{P}^2 & \cdots & \boldsymbol{P}^k & \cdots & \boldsymbol{P}^K \end{bmatrix} \tag{16}$$

$$\overleftrightarrow{\boldsymbol{T}} = \begin{bmatrix} \boldsymbol{T}^1 & \boldsymbol{T}^2 & \cdots & \boldsymbol{T}^k & \cdots & \boldsymbol{T}^K \end{bmatrix} \tag{17}$$

$$\overleftrightarrow{\boldsymbol{H}} = \begin{bmatrix} \boldsymbol{H}^{11} & & & & & \\ \boldsymbol{H}^{12} & \boldsymbol{H}^{22} & & & & \\ \vdots & \vdots & \ddots & & & \\ \boldsymbol{H}^{1k} & \boldsymbol{H}^{2k} & \cdots & \boldsymbol{H}^{kk} & & \\ \vdots & \vdots & \ddots & \vdots & \ddots & \\ \boldsymbol{H}^{1K} & \boldsymbol{H}^{2K} & \cdots & \boldsymbol{H}^{kK} & \cdots & \boldsymbol{H}^{KK} \end{bmatrix} \tag{18}$$

Eq. (15) is a linear system that relates the force components in the three directions of the N discrete forces along the blades and at different source time steps to Q microphone sound pressure at different observer time steps. Then, the force components at different locations on the fan blade planform and at different source time steps can be computed from the sampled values of the sound pressures at the measurement points by inverting Eq. (15) as:

$$\overleftrightarrow{\boldsymbol{T}} = \left(\overleftrightarrow{\boldsymbol{H}}\right)^+ \boldsymbol{P} \tag{19}$$

where the superscript "+" denotes the pseudo-inverse of a matrix.

Eq. (19) indicates that when the sound pressures at an observer time step are measured, the force components in the three directions at the corresponding source time step can be reconstructed, and thus the proposed method can realize the real-time reconstruction of the force signals. Once the force at each source point on the blade planform and at each time step is determined, the localization and quantification of the unsteady rotating loading sources can be realized. This process is herein referred to as space–time source reconstruction process.

Considering that the inverse problem is usually ill-conditioned and the source reconstruction is not straightforward, some regularization strategies, e.g., the Tikhonov regularization and the LASSO regularization, are commonly used to solve the force reconstruction problem in the time domain. Unfortunately, these conventional regularization strategies are not well suited to tackle both spatial localization and temporal reconstruction problems simultaneously, since they are generally restricted to the reconstruction of signals sharing the same space and time characteristics. A more suitable space–time regularization technique for the present inversion

problem is therefore needed, as discussed in the next subsection.

2.2. Space-time regularization

The core idea behind the space–time regularization is to exploit available prior information about the space source distribution (localized or distributed) and the nature of the source signals simultaneously. The space–time regularization with a mixed norm is introduced in the inverse problem framework [57–59], which reads:

$$\widetilde{T} = \underset{\overleftrightarrow{T}}{\arg\min} \left\| \overrightarrow{P} - \overleftrightarrow{H} \overrightarrow{T} \right\|_2^2 + \lambda \|\widehat{T}\|_{p,q}^q \tag{20}$$

where $\|\widehat{T}\|_{p,q}^q$ represents the space–time regularization term. The coefficients p and q are the norm parameters corresponding space and time, respectively. To better understand the influence of the space–time regularization during the solving process, the elements of the unknown force vector $\overrightarrow{T}$ in Eq. (17) are further rewritten into the matrix form $\widehat{T}$ as follows:

$$\widehat{T} = \begin{bmatrix} (T^1)^{\mathrm{T}} \\ (T^2)^{\mathrm{T}} \\ \vdots \\ (T^k)^{\mathrm{T}} \\ \vdots \\ (T^K)^{\mathrm{T}} \end{bmatrix}^{\mathrm{T}} = \begin{bmatrix} F_{11}^1 & F_{11}^2 & \cdots & F_{11}^k & \cdots & F_{11}^K \\ \vdots & \vdots & \ddots & \vdots & \ddots & \vdots \\ F_{N1}^1 & F_{N1}^2 & \cdots & F_{N1}^k & \cdots & F_{N1}^K \\ F_{12}^1 & F_{12}^2 & \cdots & F_{12}^k & \cdots & F_{12}^K \\ \vdots & \vdots & \ddots & \vdots & \ddots & \vdots \\ F_{N2}^1 & F_{N2}^2 & \cdots & F_{N2}^k & \cdots & F_{N2}^K \\ F_{13}^1 & F_{13}^2 & \cdots & F_{13}^k & \cdots & F_{13}^K \\ \vdots & \vdots & \ddots & \vdots & \ddots & \vdots \\ F_{N3}^1 & F_{N3}^2 & \cdots & F_{N3}^k & \cdots & F_{N3}^K \end{bmatrix} \tag{21}$$

where the rows correspond to the time signal at a particular location and the columns to the excitation field at a specific instant. N is the number of reconstruction source points of the excitation field. Consequently, by recalling that the mixed norm is defined by the following expression:

$$\|\widehat{T}\|_{p,q}^q = \sum_{k=1}^K \left(\sum_{i=1}^3 \sum_{n=1}^N |F_{ni}^k|^p \right)^{\frac{q}{p}} \tag{22}$$

it is clear that the regularization term introduces an explicit coupling between the coefficients of $\widehat{T}$ and allows promoting some structures observed in real signals [60]. To illustrate this particular property of the mixed norms, let us consider the case for which $p = 1$ and $q = 2$. In this situation, the matrix $\widehat{T}$ is supposed to be sparse along the lines (space) and full along the rows (time). In other words, by using this setting, we can promote the spatial sparsity of the excitation field and the continuity of the time signals. We can therefore argue that the space–time regularization is highly flexible, since it allows dealing with various force distributions and various excitation signals within a unique framework.

The minimization problem in Eq. (20) can be solved by the generalized iterative reweighted least squares algorithm [61,62] by transforming $\|\widehat{T}\|_{p,q}^q$ to $\left\| \widehat{W} \overrightarrow{T} \right\|_2^2$, which reads:

$$\widetilde{T} = \underset{\overleftrightarrow{T}}{\arg\min} \left\| \overrightarrow{P} - \overleftrightarrow{H} \overrightarrow{T} \right\|_2^2 + \lambda \left\| \widehat{W} \overrightarrow{T} \right\|_2^2 \tag{23}$$

where $\widehat{W}$ is a diagonal matrix and its element is $\sqrt{W_{ni}^k W^k}$.

$$W_{ni}^k = \begin{cases} |F_{ni}^k|^{p-2} & , |F_{ni}^k| \geqslant \varepsilon \\ \varepsilon^{p-2} & , \text{otherwise} \end{cases} \tag{24}$$

$$W^k = \begin{cases} \left[\left\| (T^k)^{\mathrm{T}} \right\|_p^p \right]^{q/p-1} & , \left\| (T^k)^{\mathrm{T}} \right\|_p^p \geqslant \varepsilon^2 \\ (\varepsilon^2)^{q/p-1} & , \text{otherwise} \end{cases} \tag{25}$$

In Eqs. (24) and (25), a small real positive number ε is added to W_{ni}^k and W^k, respectively, to avoid infinite weights. The explicit solution of Eq. (23) can be expressed in the following form:

$$\widetilde{T} = \left(\overrightarrow{H}^{\,H} \overleftrightarrow{H} + \lambda \overleftrightarrow{W} \right)^{-1} \overleftrightarrow{H}^{\,H} \overleftrightarrow{P} \tag{26}$$

where $\overleftrightarrow{W} = \widehat{W}^{H} \widehat{W}$, with the superscript "H" denoting the Hermitian transpose.

Since the weighting matrix $\overleftrightarrow{W}$ depends on the exciting force F_{ni}^{k} based on Eqs. (24) and (25), an iterative process must be employed to solve the minimization problem. The solution $\widetilde{T}^{(s)}$ at iteration s relies on solution at iteration $s-1$, namely:

$$\widetilde{T}^{(s)} = \left(\overleftrightarrow{H}^{\,H} \overleftrightarrow{H} + \lambda \overleftrightarrow{W}^{(s-1)} \right)^{-1} \overleftrightarrow{H}^{\,H} \overleftrightarrow{P} \tag{27}$$

where the weighting matrix $\overleftrightarrow{W}^{(s-1)}$ at iteration $s-1$ is based on the exciting force F_{ni}^{k} at iteration $s-1$. The initial solution of the iterative procedure is estimated based on the standard Tikhonov regularization [63] which corresponds to $p = q = 2$, i.e.:

$$\widetilde{T}^{(0)} = \underset{\overleftrightarrow{T}}{\mathrm{argmin}} \left\| \overleftrightarrow{P} - \overleftrightarrow{H} \overleftrightarrow{T} \right\|_{2}^{2} + \lambda \left\| \overleftrightarrow{T} \right\|_{2}^{2} \tag{28}$$

or, in an explicit form, to:

$$\widetilde{T}^{(0)} = \left(\overleftrightarrow{H}^{\,H} \overleftrightarrow{H} + \lambda I \right)^{-1} \overleftrightarrow{H}^{\,H} \overleftrightarrow{P} \tag{29}$$

where $\widetilde{T}^{(0)}$ is the initial solution, I stands for a unit matrix, and λ is determined according to the L-curve criterion [64]. The functional J at iteration s is given by

$$J\left(\widetilde{T}^{(s)}\right) = \left\| \overleftrightarrow{P} - \overleftrightarrow{H} \widetilde{T}^{(s)} \right\|_{2}^{2} + \lambda \left\| \overleftrightarrow{W}^{(s-1)} \widetilde{T}^{(s)} \right\|_{2}^{2} \tag{30}$$

As a result, the relative variation δ of the functional J between two adjacent iterations can be expressed as:

$$\delta = \left| 1 - \frac{J\left(\widetilde{T}^{(s)}\right)}{J\left(\widetilde{T}^{(s-1)}\right)} \right| \tag{31}$$

The algorithm is stopped when the relative variation between two iterations is less than or equal to a given tolerance or when the maximum number of iterations is reached.

It is worth noting that in real-life applications, finding proper values for p and q is not straightforward, because the force distribution is unknown. Some guidelines, based on some research experience [24,30,60,62] and the existing literature on convex and non-convex optimizations [27,52,63], can be used. As a rule of thumb, if the excitation field is supposed to be uniform in space, then it is reasonable to set $p = 2$. On the contrary, if the excitation field is rather localized, then choosing $p \leqslant 1$ allows promoting the sparsity of the solution. A prior knowledge of excitation signal can be also used, in particular, it is reasonable to set $q = 2$ if the time signal is supposed to be continuous over the considered duration, while $q \leqslant 1$ if the signal is rather impulsive.

Since the main focus of the present research is on the noise generated by thin blades rotating at subsonic tip speed, the aerodynamic forces concentrated in the blade tip region are the dominant noise sources. On the other hand, when the rotor operates in quasi-
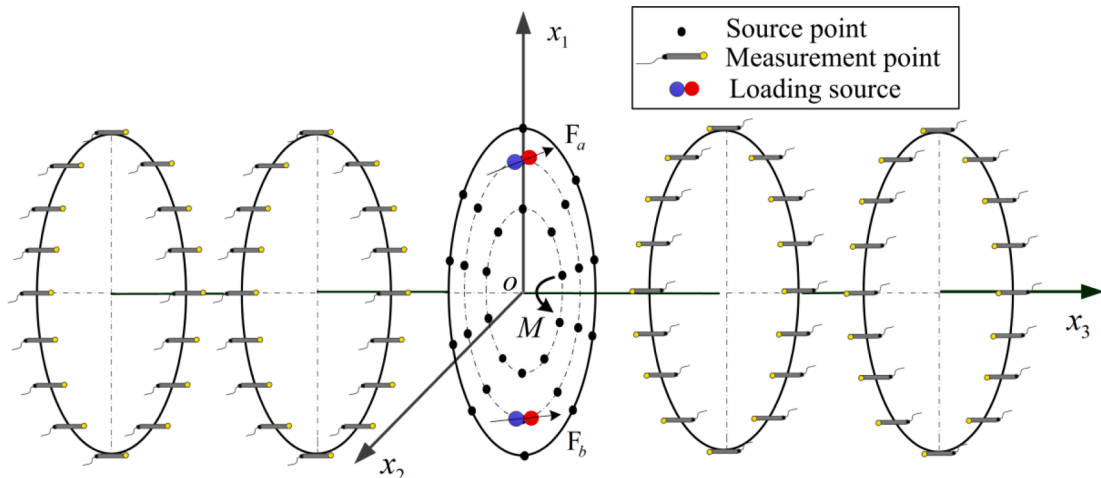

Fig. 2. Geometric description of the rotating loading sources, source points and measurement points.

quiescent conditions or even in non-axial flow conditions and does not incur in strong blade-vortex interaction conditions, the noise signals are rather smooth in time. In this situation, setting $p \leqslant 1$ and $q = 2$ is a meaningful choice, because the method takes advantage of the spatial sparsity of the excitation field and allows promoting the sparsity of the solution by choosing an l_p-norm in space ($p \leqslant 1$). This allows to improve the reconstruction accuracy of the forces when the number of measurement points is less than that of unknowns.

3. Numerical validation of the method

In this section, numerically computed sound pressure signals are used as an input of the inverse problem to analyze the performance of the ST-TDIM in reconstructing the unsteady rotating forces and to compare the reconstruction results of the C-TDIM and the ST-TDIM in two different cases, also including undersampling conditions and oversampling conditions. The layout of source points in the simulation is shown in Fig. 2, a series of source points are distributed on three rings with the radii of 0.1, 0.2 and 0.3 m, and each ring contains ten source points. These source points have identical rotational speed. It is worth pointing out that, in this specific case, the second ring radius coincides with the radial location of two "real" point forces located at the initial positions F_a (0.2, 0, 0) m and F_b (-0.2, 0, 0) m in the reference system $o(x_1, x_2, x_3)$ centered at the rotation center. This choice allows to a more insightful verification of the method, since the space sparsity of the solution is fully recovered.

For quantifying the accuracies of the ST-TDIM and the C-TDIM, the phase evaluation factor E_p and the amplitude evaluation factor E_a are used as accuracy/error indicators, which are defined as [65]:

$$E_p = \frac{\left| \boldsymbol{F}_{\text{th}}^{\text{T}} \boldsymbol{F}_{\text{re}} \right|}{\sqrt{\left(\boldsymbol{F}_{\text{th}}^{\text{T}} \boldsymbol{F}_{\text{th}} \right) \left(\boldsymbol{F}_{\text{re}}^{\text{T}} \boldsymbol{F}_{\text{re}} \right)}}, \tag{32}$$

$$E_a = \frac{\left| \sqrt{\boldsymbol{F}_{\text{th}}^{\text{T}} \boldsymbol{F}_{\text{th}}} - \sqrt{\boldsymbol{F}_{\text{re}}^{\text{T}} \boldsymbol{F}_{\text{re}}} \right|}{\sqrt{\boldsymbol{F}_{\text{re}}^{\text{T}} \boldsymbol{F}_{\text{re}}}}, \tag{33}$$
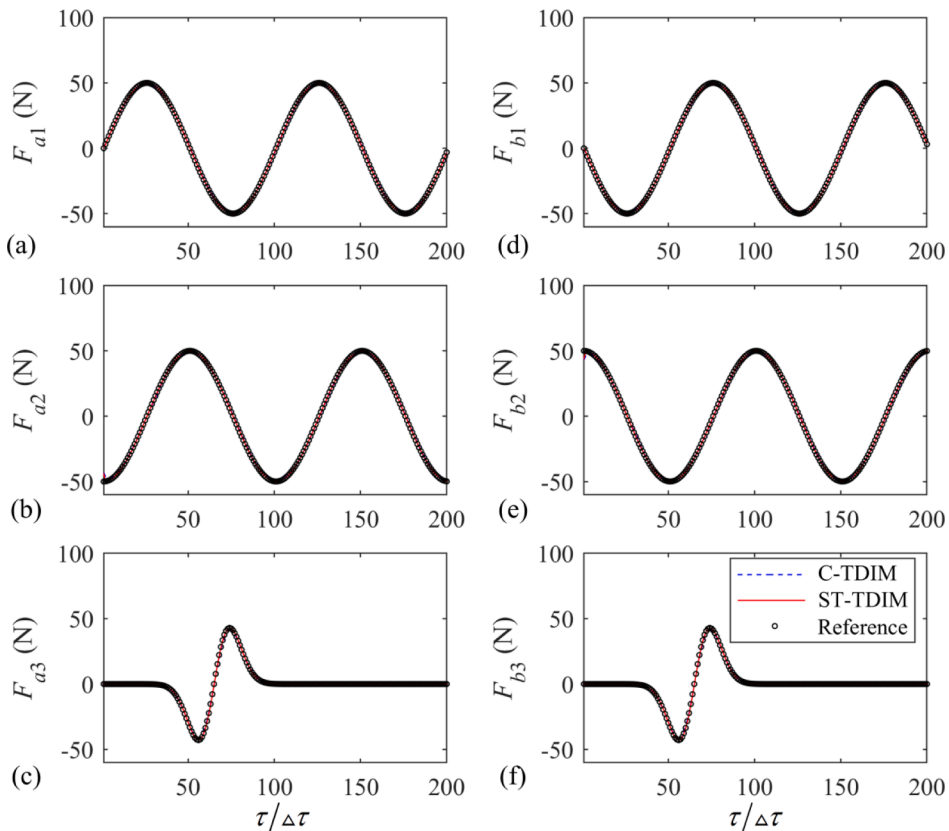
Fig. 3. Comparison of the reconstructed and reference force components of rotating loading sources: (a) the x_1 direction components of F_a; (b) the x_2 direction components of F_a; (c) the x_3 direction components of F_a; (d) the x_1 direction components of F_b; (e) the x_2 direction components of F_b; (f) the x_3 direction components of F_b.

where the superscript "T" denotes the transpose of matrix; F_{th} and F_{re} are the theoretical and reconstructed forces, respectively; E_p indicates the phase similarity that should tend to 1, and E_a indicates the amplitude difference that should tend to 0. In the simulations, three components of theoretical forces on the two unsteady rotating loading sources F_a^{th} and F_b^{th} in the Cartesian coordinate system $o(x_1, x_2, x_3)$ are prescribed as:

$$F_a^{th} \begin{cases} F_{a1}^{th} = F_D\sin(\phi_1 + \Omega\tau) \\ F_{a2}^{th} = -F_D\cos(\phi_1 + \Omega\tau) \\ F_{a3}^{th} = F_L = C((\tau - \tau_o)/T_v)\exp(-(\tau - \tau_o)^2/T_v^2) \end{cases} \tag{34}$$

$$F_b^{th} \begin{cases} F_{b1}^{th} = F_D\sin(\phi_2 + \Omega\tau) \\ F_{b2}^{th} = -F_D\cos(\phi_2 + \Omega\tau) \\ F_{b3}^{th} = F_L = C((\tau - \tau_o)/T_v)\exp(-(\tau - \tau_o)^2/T_v^2) \end{cases} \tag{35}$$

where ϕ_1 and ϕ_2 are the initial phases of the two unsteady rotating loading sources, respectively; F_D is the magnitude of the drag force; F_L is the magnitude of the thrust force; C is a constant number; τ_o is the pulse time delay and T_v is the pulse time spreading width. The specific parameter values are given as $F_D = 50$ N, $C = 100$, $\phi_1 = 0$, $\phi_2 = \pi$, $\Omega = 2\pi\widehat{N}/60$, $\widehat{N} = 1020$ rpm, $\tau_o = 64\Delta t$, and $T_v = 12.8\Delta t$ with the time step $\Delta t = 1/1700$ s, where the sampling frequency is 1700 Hz.

3.1. Case 1: Oversampling conditions

In order to analyze the performance of the ST-TDIM and the C-TDIM under oversampling conditions, 120 sampling points are first used to reconstruct the unsteady rotating forces. In this situation, 90 unknowns (30×3 force components) must be determined from 120 measurement points. The measurement array is arranged as shown in Fig. 2, which is set as multiple rings of the same radius of 0.25 m located on planes parallel to the rotor disk, and each ring contains 30 measurement points. The position of each ring in the x_3
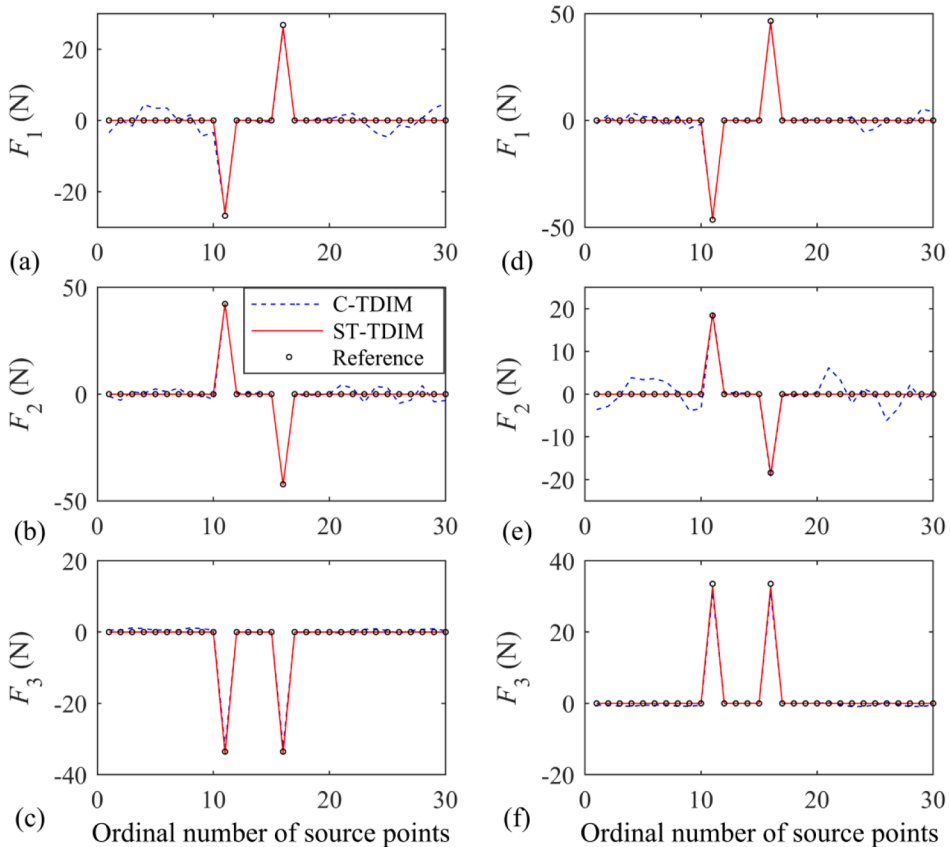
Fig. 4. Comparison of the reconstructed and reference force components F_1, F_2 and F_3 at all source points: (a) F_1 at the selected time step τ_{60}; (b) F_2 at the selected time step τ_{60}; (c) F_3 at the selected time step τ_{60}; (d) F_1 at the selected time step τ_{70}; (e) F_2 at the selected time step τ_{70}; (f) F_3 at the selected time step τ_{70}.

direction is set to be −0.04 m, −0.02 m, 0.02 m, and 0.04 m. Additional Gaussian white noise with a signal-to-noise ratio of 30 dB is added to the pressure signals for simulating more realistic conditions. Since the real values of two rotating loading sources are known in the simulation, they are used as the references for comparison.

Fig. 3 shows the time histories of the unsteady rotating forces reconstructed by the ST-TDIM and the C-TDIM and compared to the reference ones. It can be argued that, in the case of sufficient sampling points, the three direction components of unsteady rotating forces reconstructed by the two methods are in good agreement with the reference values during the entire time period. Furthermore, based on Eq. (32) and Eq. (33), the phase indicators E_p and the amplitude indicators E_a of the reconstructed unsteady rotating forces can be further evaluated. The phase indicator for the C-TDIM is 0.0194 (same value for the two point forces), whereas the amplitude indicator is 0.9999. The phase indicator for the ST-TDIM is 0.0028, whereas the amplitude indicator is 0.9999. Compared with the C-TDIM, the ST-TDIM can achieve slightly higher temporal reconstruction accuracy of the unsteady rotating forces in oversampling conditions.

Additionally, detailed information of the unsteady rotating forces reconstructed by the two methods at all source points and at two selected time steps are reported in Fig. 4. The reference force values are plotted for a qualitative visual evaluation of the reconstruction accuracy. It can be argued that both the ST-TDIM and C-TDIM can reconstruct the unsteady rotating forces, but the ST-TDIM is slightly more accurate than the C-TDIM in reconstructing the force components in the three directions at all source points.

In order to better visualize the spatial localization results of the two methods, the source maps at the time steps of τ_{26} and τ_{101} are shown in Fig. 5. It can be pointed out that the C-TDIM can accurately localize the locations of the unsteady rotating loading sources at different time steps, but some side lobes appear in the map. Conversely, the source maps obtained by the ST-TDIM are significantly cleaner.

All these results indicate that, under oversampling conditions, the ST-TDIM can solve both the spatial and temporal reconstruction problems of unsteady rotating forces slightly more accurately than the C-TDIM, thanks to a prior knowledge of space and time characteristics of the forces.

3.2. Case 2: Undersampling conditions

Although both the ST-TDIM and the C-TDIM can obtain accurate results under oversampling conditions, the two methods are essentially different. The ST-TDIM introduces a space–time regularization with a mixed norm in the inverse problem framework, which can tackle both spatial and temporal reconstruction problems of the unsteady rotating forces, simultaneously. Furthermore, unlike the C-TDIM, the ST-TDIM can take advantage of a prior knowledge of the space–time characteristics of the unsteady rotating forces and enhance the sparseness of the solution and reduce the computational cost of the inversion.

In order to stress the capability of the new method in undersampling conditions, in this subsection, 48 sampling points are used to compare the accuracies of the two methods. In this situation, 90 unknowns (30×3 force components) must be determined from 48
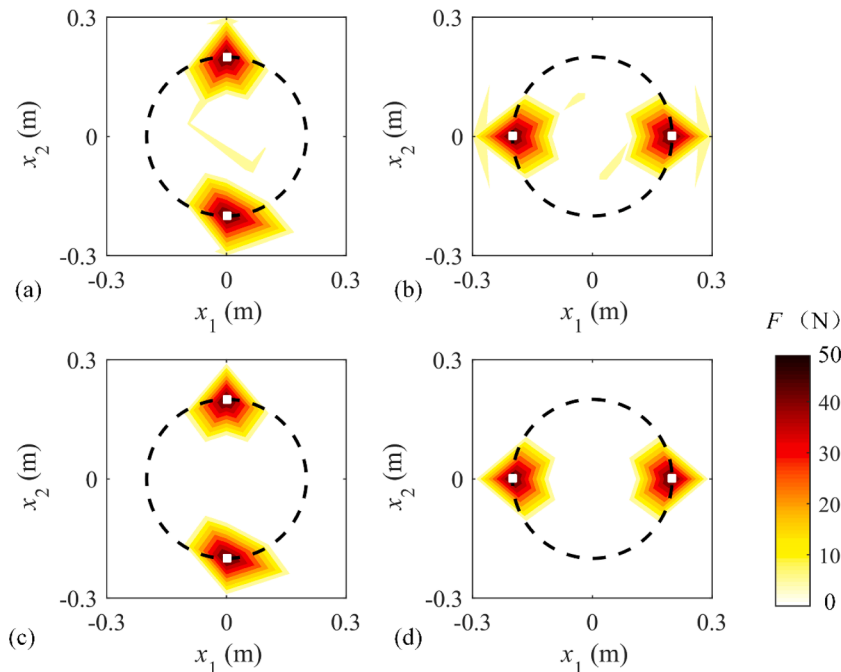

Fig. 5. Spatial distribution of the reconstructed forces (a) by the C-TDIM at time step τ_{26}; (b) by the C-TDIM at time step τ_{101}; (c) by the ST-TDIM at time step τ_{26}; (d) by the ST-TDIM at time step τ_{101}. The white squares indicate the real positions of two rotating loading sources, F indicates the total force.

measurement points. The arrangement of the measurement array is the same as for Case 1, but each ring contains only 12 measurement points. Other simulation parameters are the same as those in Case 1.

Fig. 6 shows the comparison of the time variation of the reconstructed forces and the reference values. It can be argued that when the number of sampling points is reduced to 48, differences between the two methods are remarkable, with a clearly higher accuracy achieved by the ST-TDIM. Furthermore, the phase indicators are 0.2281 and 0.0053 for the C-TDIM and ST-TDIM, respectively, whereas the amplitude indicators are 0.9920 and 0.9999, respectively. The higher accuracy of the ST-TDIM is confirmed by these figures.

At all source points, the unsteady rotating force components reconstructed by the ST-TDIM and the C-TDIM are compared with the theoretical values at two selected time steps, as shown in Fig. 7. It can be seen that the force components at different source points reconstructed by the ST-TDIM are remarkably similar to the theoretical ones, while the reconstructed results of the C-TDIM exhibit higher discrepancies with respect to the reference values.

The source maps obtained by the two methods at the time steps of τ_{26} and τ_{101} are finally presented in Fig. 8. The maps obtained using the two methods are rather continuous. However, the C-TDIM results exhibit a more smeared pattern and several side lobes. Conversely, the unsteady rotating forces reconstructed by the ST-TDIM are more concentrated in space at the effective locations.

In practical usage of the inversion method, fewer sampling points mean lower computational cost and lower reconstruction accuracy. Therefore, it is interesting to investigate the convergence characteristics of the two methods by estimating the accuracy indicators for increasing number of sampling points, from 16 to 120. Fig. 9 shows the phase and amplitude indicators obtained for different sampling points. Both methods exhibit a consistent behavior, with indicators reviling an increasing accuracy as the number of sampling points is increased. When 20 sampling points are used, the phase indicator for the C-TDIM is close to 0.8 and the amplitude indicator is close to 0.6, whereas a significantly more accurate reconstruction is achieved by the ST-TDIM, which appears to be much more robust. Even when only 16 measurement points are used, the ST-TDIM yields satisfactory results. As the number of sampling points is increased, the C-TDIM error indicators tend to approach the values of the ST-TDIM, but the accuracy is always lower. When 90 sampling points are used, the number of equations to solve the force components is the same as the number of unknown force components, both phase indicators are close to 1 and the amplitude indicators are close to 0, which indicates that both methods can obtain satisfactory reconstruction accuracy under oversampling conditions.

In addition, in order to study the effects of noise on the two methods, the accuracy indicators of the two methods in reconstructing
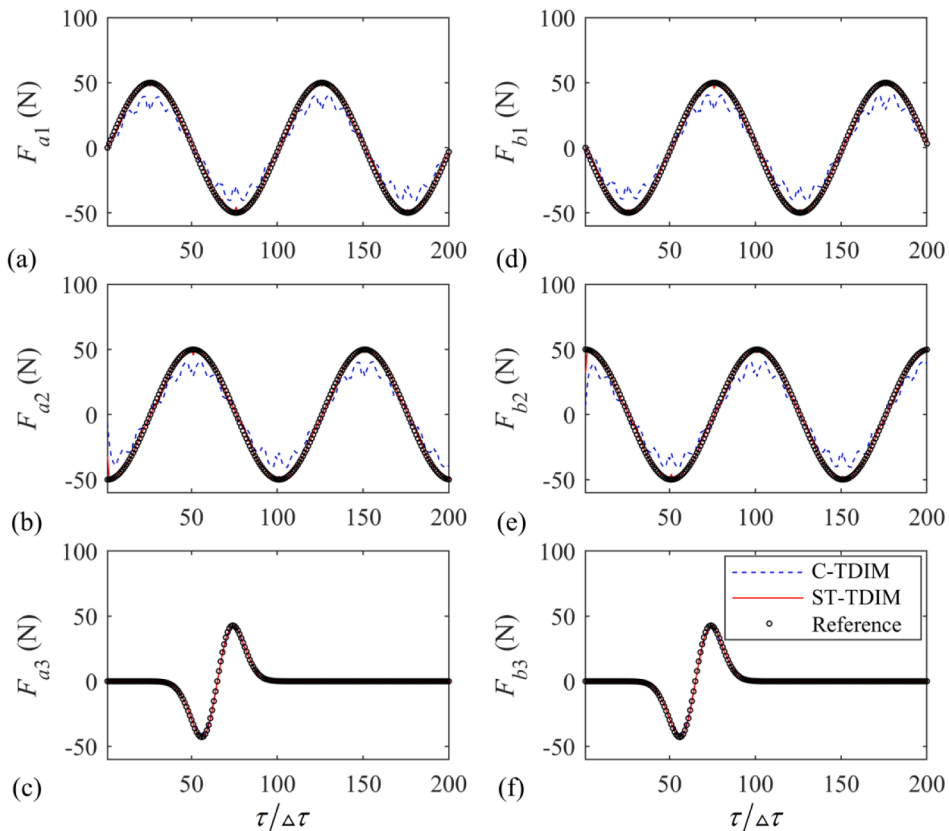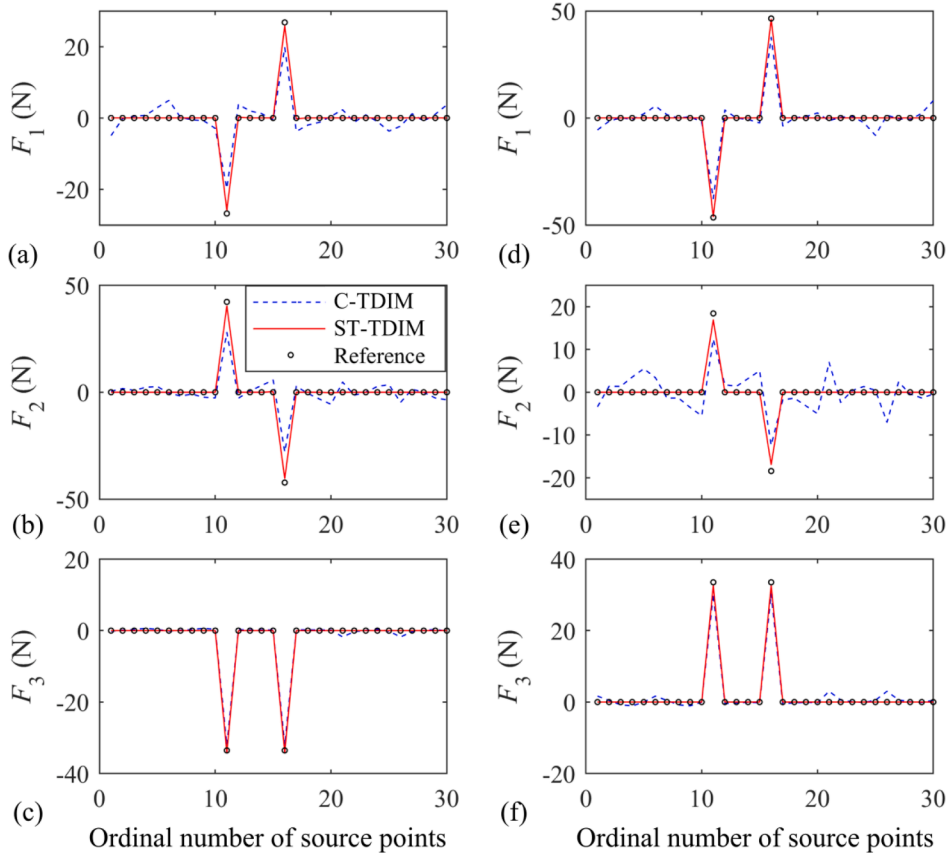

Fig. 6. Comparison of the reconstructed and reference strength components of rotating loading sources: (a) the x_1 direction components of F_a; (b) the x_2 direction components of F_a; (c) the x_3 direction components of F_a; (d) the x_1 direction components of F_b; (e) the x_2 direction components of F_b; (f) the x_3 direction components of F_b.

Fig. 7. Comparison of the reconstructed and reference force components F_1, F_2 and F_3 at all source points: (a) F_1 at the selected time step τ_{60}; (b) F_2 at the selected time step τ_{60}; (c) F_3 at the selected time step τ_{60}; (d) F_1 at the selected time step τ_{70}; (e) F_2 at the selected time step τ_{70}; (f) F_3 at the selected time step τ_{70}.

the unsteady rotating forces at different signal-to-noise ratios (SNRs), in the range from 0 dB to 30 dB, are calculated, as shown in Fig. 10. It can be observed that with the decrease of SNRs, the influences of noise on the phase indicators and the amplitude indicators of the two methods are slight, and the performance of the proposed method in reconstructing the unsteady rotating forces at different SNRs is always better than that of the C-TDIM, thanks to a prior knowledge of space and time characteristics of the forces.

4. Experimental validation of the method

In this section, the reconstruction methods are validated by using, as an input, real measurements of noise signals radiated from a small rotor. Experiments were carried out in a semi-anechoic chamber. The experimental setup was shown in Fig. 11. An UAV carbon fiber rotor was used. The rotor diameter was 0.4 m, the blade thickness was about 0.001 m, and the blade chord at 80% of tip radius was 0.025 m. The drive system was constituted by a low-noise direct current brushless motor. A laser speedometer is used to measure the blade tip speed, which is 999 rpm, corresponding to a tip Mach number of 0.0615. As sketched in Fig. 12, the blade planform was discretized into a series of source points. These source points were distributed along three rings with the radii of 0.1 m, 0.2 m and 0.4 m. Each ring contained 10 points. The loading sources at these points were supposed to rotate at the same rotational speed as the blade.

An array of double rings side by side containing 60 omnidirectional microphones (BSWA MPA 451) in total (30 × 2) was used to perform the measurements. The diameter of the array is 0.5 m. Two measurements were carried out for two axial positions of the double array, corresponding to the following axial distances of the microphone rings from the rotor disk: 0.02 m, 0.03 m and 0.04 m, 0.05 m, 120 sampling points were obtained, as shown in Fig. 12. To guarantee that the sound fields of the two measurements were the same, the pulse signals measured by the laser speedometer were set as the triggers to activate the acquisition system recording the data. A Müller-BBM acquisition instrument with 60-bit cards is used to simultaneously sample the sound pressure signals at 60 microphone locations, and the sampling frequency is 10.24 kHz.

4.1. Oversampling conditions

In order to analyze the performance of the ST-TDIM and C-TDIM under oversampling conditions from the perspective of
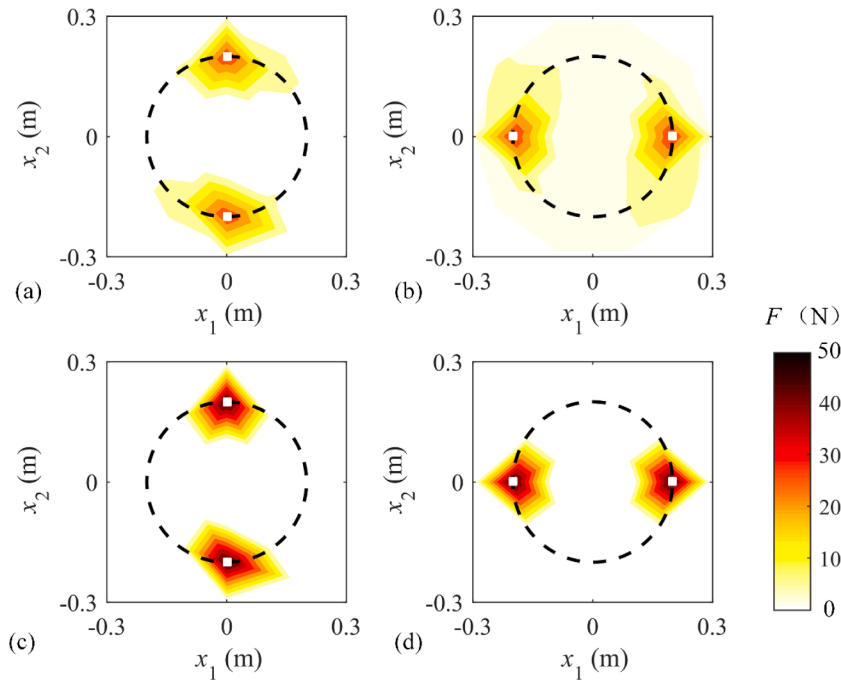
Fig. 8. Spatial distribution of the reconstructed forces: (a) by the C-TDIM at time step τ_{26}; (b) by the C-TDIM at time step τ_{101}; (c) by the ST-TDIM at time step τ_{26}; (d) by the ST-TDIM at time step τ_{101}. The white squares indicate the real positions of two rotating loading sources, F indicates the total force.
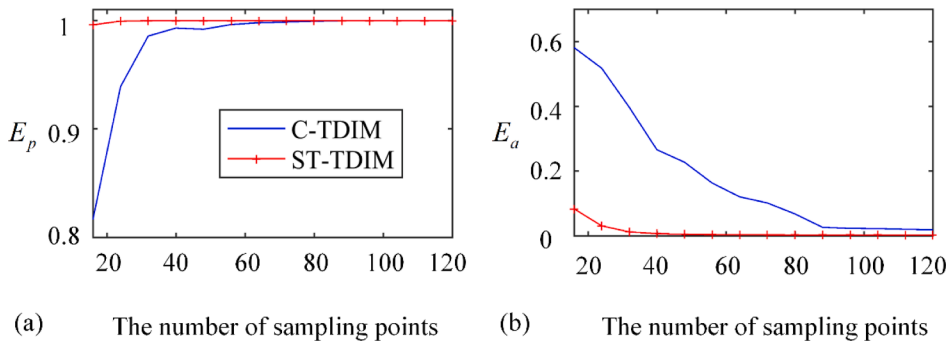
Fig. 9. The phase indicators E_p (a) and the amplitude indicators E_a (b) of the unsteady rotating forces at different sampling points.
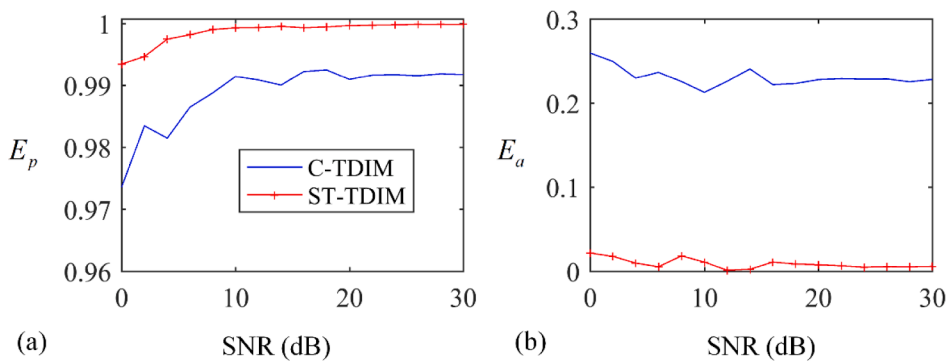
Fig. 10. The phase indicators E_p (a) and the amplitude indicators E_a (b) of the unsteady rotating forces at different SNRs when 48 sampling points are used.
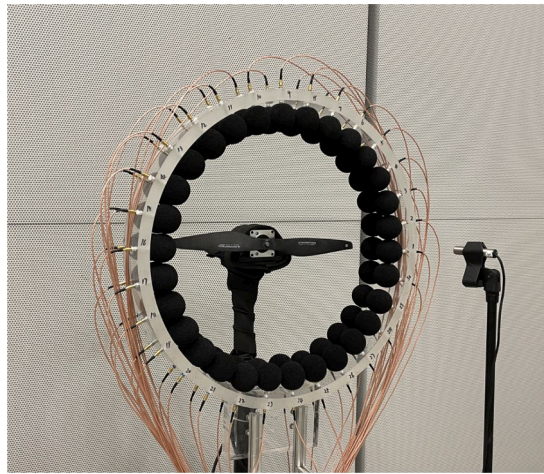
Fig. 11. Experimental setups for measuring the UAV rotating blade noise: the UAV blades and the microphone array, and the laser speedometer.
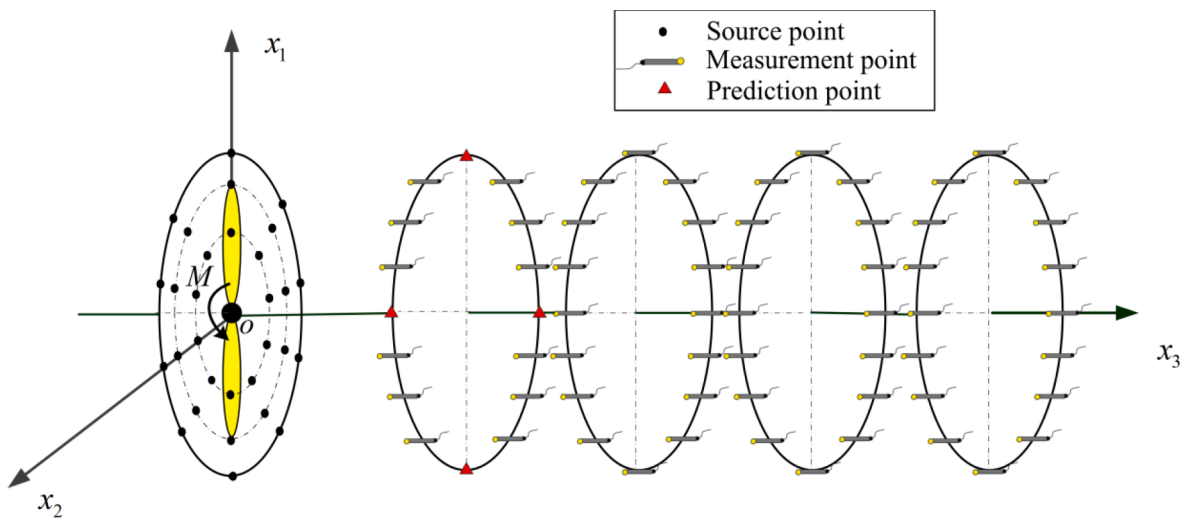
Fig. 12. Geometric description of the rotating blades, source points, measurement points and prediction points.

experiments, 116 sampling points on sub-arrays at the positions 0.02 m, 0.03 m, 0.04 m and 0.05 m shown in Fig. 12 were first used to reconstruct the rotating forces.

Fig. 13 shows the localization results of the ST-TDIM and the C-TDIM for the two rotating blades at two different time steps τ_{460} and τ_{615}. It can be seen that although the two methods can localize the loading sources on the rotating blades at different time steps clearly under oversampling conditions, the ST-TDIM can obtain clearer source maps than the C-TDIM. The loading sources mainly concentrate at the tips of the blades, where the rate of change of the Mach number projected in the observer direction is largest at this radius and the velocity is higher, corresponding to higher force magnitudes. As expected, the loading sources in the blade tip region are the most significant part of the signature. From these results, it can be asserted that the ST-TDIM can achieve accurate source localizations at different time steps in the case of sufficient sampling points.

Fig. 14 shows the time histories of unsteady rotating forces reconstructed by the ST-TDIM and C-TDIM at 116 sampling points. It is clear that, when a sufficient number of sampling points is used, the unsteady rotating forces reconstructed by the two methods are similar. As expected, the reconstructed force components in both x_1 and x_2 directions exhibit the sine and cosine harmonic form due to the projection of the drag force component at different azimuthal locations of the blade. The difference between the initial phases of the unsteady forces on two rotating blades is 180 degrees. In addition, it can be observed that the time average reconstructed force components in the x_3 direction is negative, meaning that it is a positive thrust component applied to the blade. There are periodic fluctuations in force components in the x_3 direction when the blade is interacting with the unsteady wake, or vortex [54].

Considering that the C-TDIM can accurately reconstruct the unsteady rotating forces on the rotating blade under oversampling conditions [43], the present results confirm that also the ST-TDIM can accurately reconstruct the unsteady rotating forces in similar conditions.
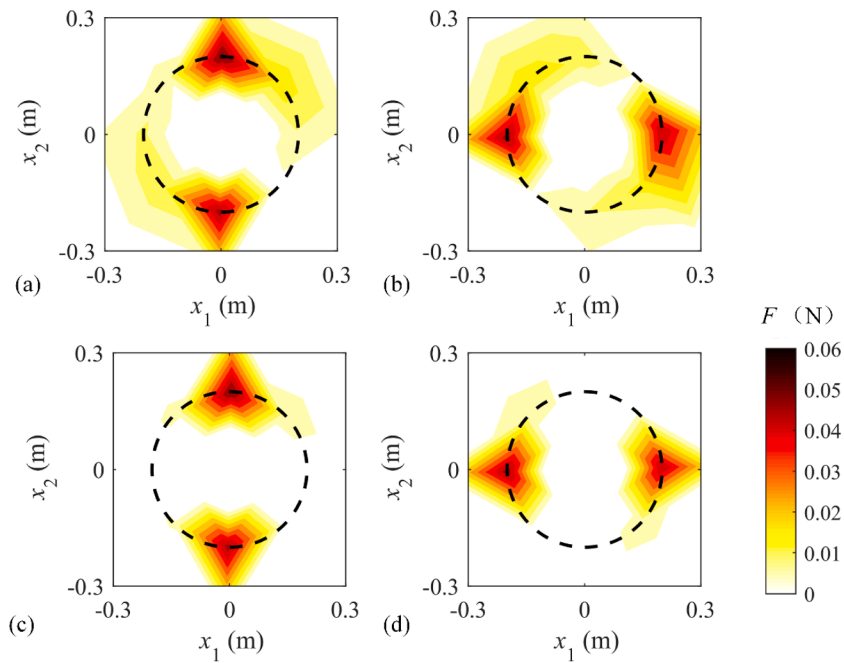
Fig. 13. The localization results of the two rotating blades (a) by the C-TDIM at time step τ_{460}; (b) by the C-TDIM at time step τ_{615}; (c) by the ST-TDIM at time step τ_{460}; (d) by the ST-TDIM at time step τ_{615}, F indicates the total force.
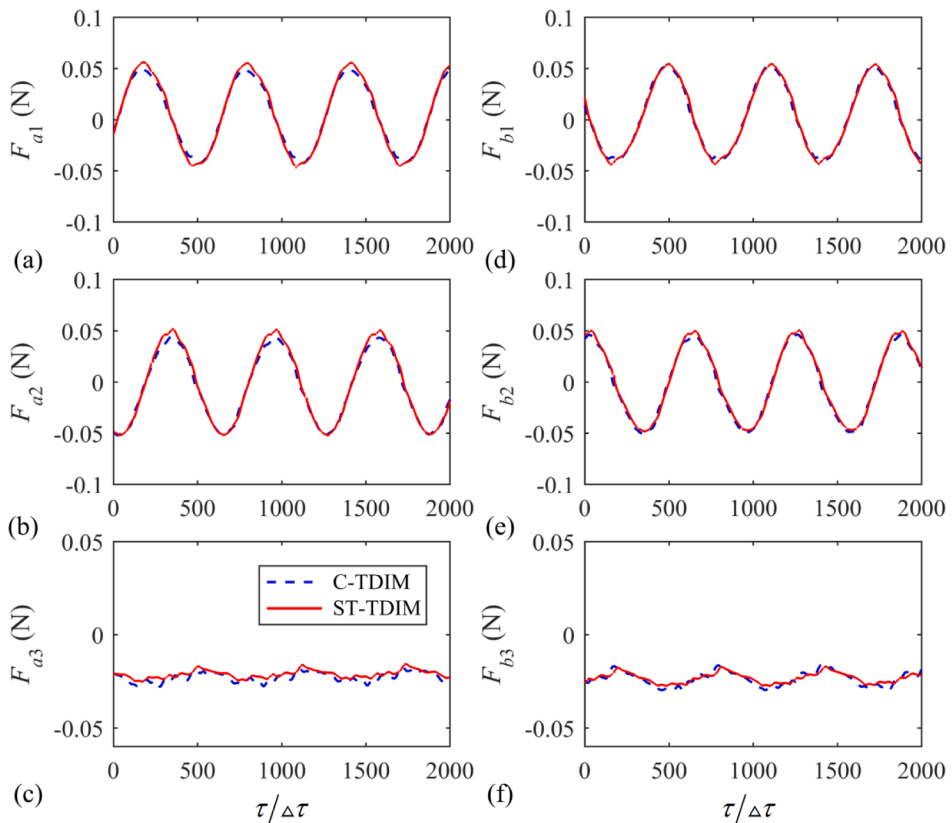

Fig. 14. The reconstructed strength components in the three directions on the tip of two rotating blades: (a) the x_1 direction components of F_a; (b) the x_2 direction components of F_a; (c) the x_3 direction components of F_a; (d) the x_1 direction components of F_b; (e) the x_2 direction components of F_b; (f) the x_3 direction components of F_b.

The reconstruction accuracy of the proposed method is further evaluated by comparing the predicted sound field based on the reconstruction forces with the measured ones. Fig. 15 shows the comparison of sound pressures at four prediction points M1 (0.2, 0, 0.02) m, M2 (0, 0.2, 0.02) m, M3 (-0.2, 0, 0.02) m, and M4 (0, −0.2, 0.02) m. It can be seen that the results predicted by the ST-TDIM and C-TDIM are in good agreement with the measured ones, except for the slight oscillations in the amplitudes of the pressure signals. Furthermore, the phase indicators E_p and the amplitude indicators E_a of sound pressures at the prediction point M1 are calculated to evaluate the accuracy of the predicted pressures based on the ST-TDIM and C-TDIM. E_p and E_a for the ST-TDIM are 0.9163 and 0.0126, respectively, while those for the C-TDIM are 0.8965 and 0.0646, respectively. Therefore, the ST-TDIM performs slightly better than the C-TDIM in the present validation case.

4.2. Undersampling conditions

Similarly to the analysis carried out using numerical signals, 45 sampling points are used in the experiment to analyze the performance of the two methods. The data of 45 sampling points are uniformly selected from the sound pressure data of the 90 sampling points at the positions 0.03 m, 0.04 m and 0.05 m, by using only 15 measurement points per ring. Other settings remain unchanged.

The source maps obtained by of the ST-TDIM and C-TDIM in undersampling conditions at the time steps τ_{460} and τ_{615} are presented in Fig. 16. Both methods are able to predict the source locations, but the C-TDIM exhibit side lobes and its spatial resolution is lower. Compared to the previous oversampling results, the accuracy of the C-TDIM is significantly lower, whereas the ST-TDIM performs similarly, except for the presence of few minor side lobes.

Fig. 17 shows the time histories of the unsteady rotating forces reconstructed by the ST-TDIM and the C-TDIM with 45 sampling points. It can be seen that the unsteady rotating force signals reconstructed by the C-TDIM are less smooth and the force fluctuations exhibit significantly lower amplitudes than in oversampling conditions (Fig. 14). Conversely, the ST-TDIM results present similar accuracy as in oversampling conditions.

In order to further evaluate the accuracy of the two methods in undersampling condition, Fig. 18 shows the comparison of the predicted sound pressures at four different prediction points M1 (0.2, 0, 0.02) m, M2 (0, 0.2, 0.02) m, M3 (-0.2, 0, 0.02) m and M4 (0, −0.2, 0.02) m. It is clear that the ST-TDIM predictions are in much better agreement with the measurements. The phase and amplitude indicators at the prediction point M1 are calculated. The phase indicators are 0.9075 and 0.8505 for the ST-TDIM and C-TDIM, respectively, whereas the amplitude indicators are 0.0826 and 0.5865, respectively. A clearly higher accuracy is thus achieved by the ST-TDIM. This conforms that, also in a realistic usage scenario, the proposed method performs better than the conventional one.

5. Conclusions

A time-domain inverse method based on a space–time regularization with a mixed norm has been presented and validated. The method allows to calculate unsteady forces acting on rotor blades from microphone array measurements. The proposed method takes
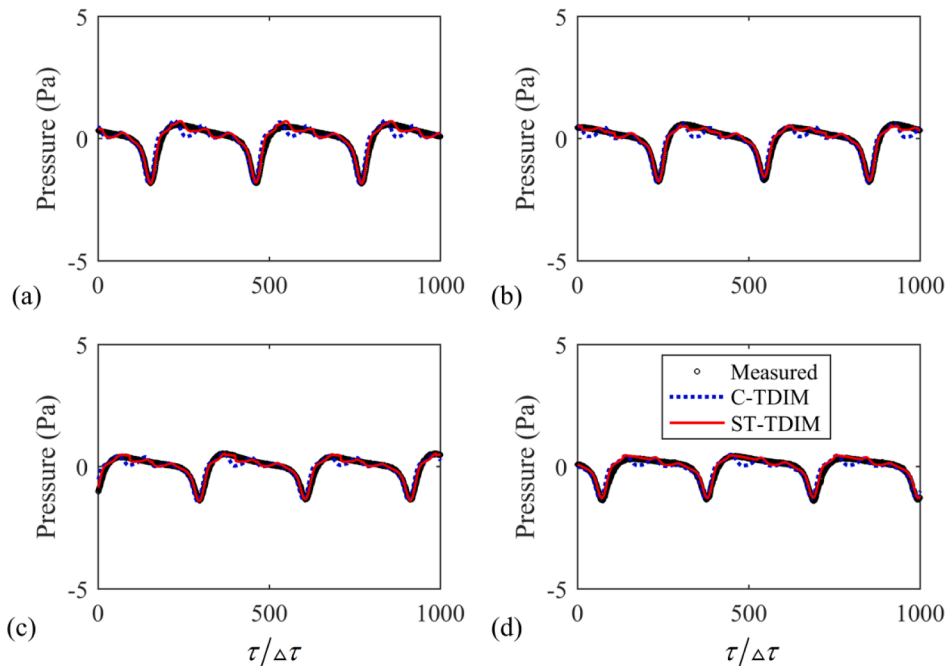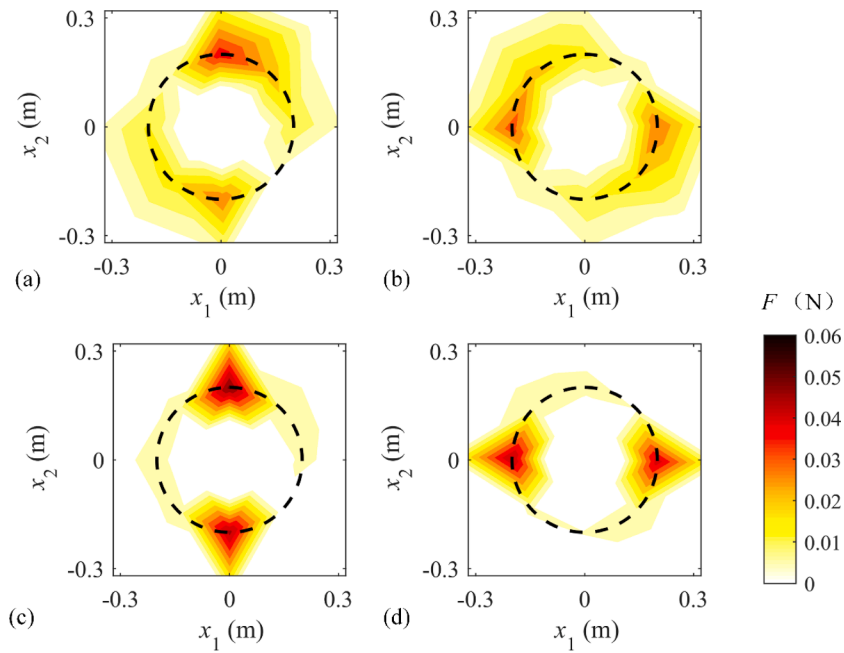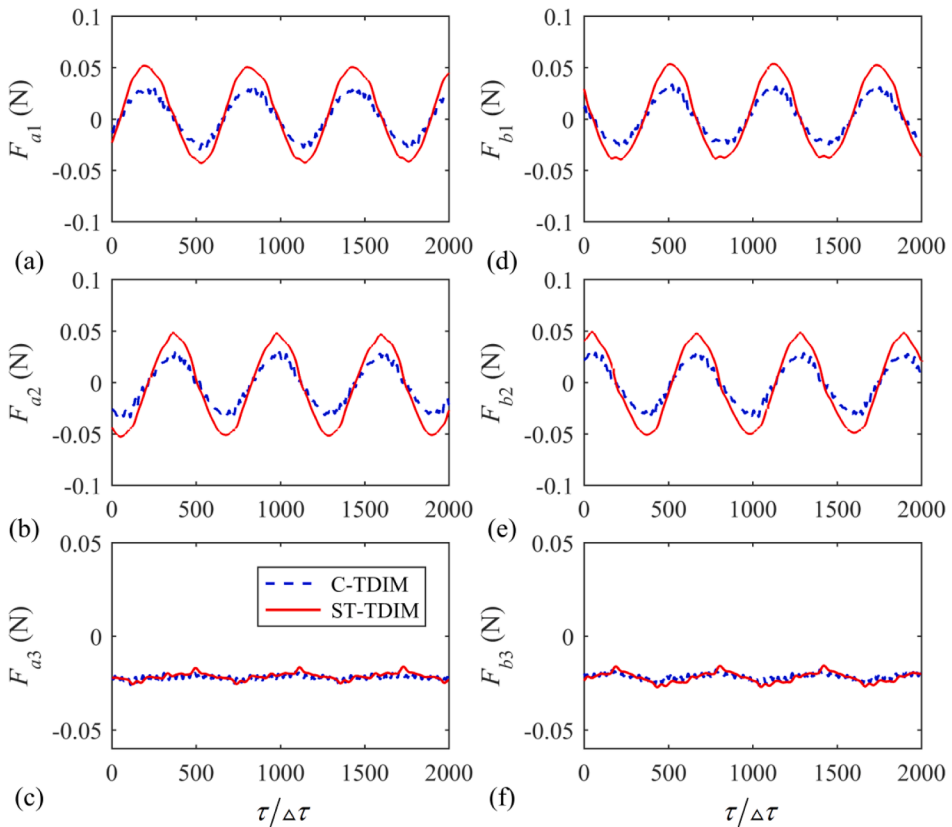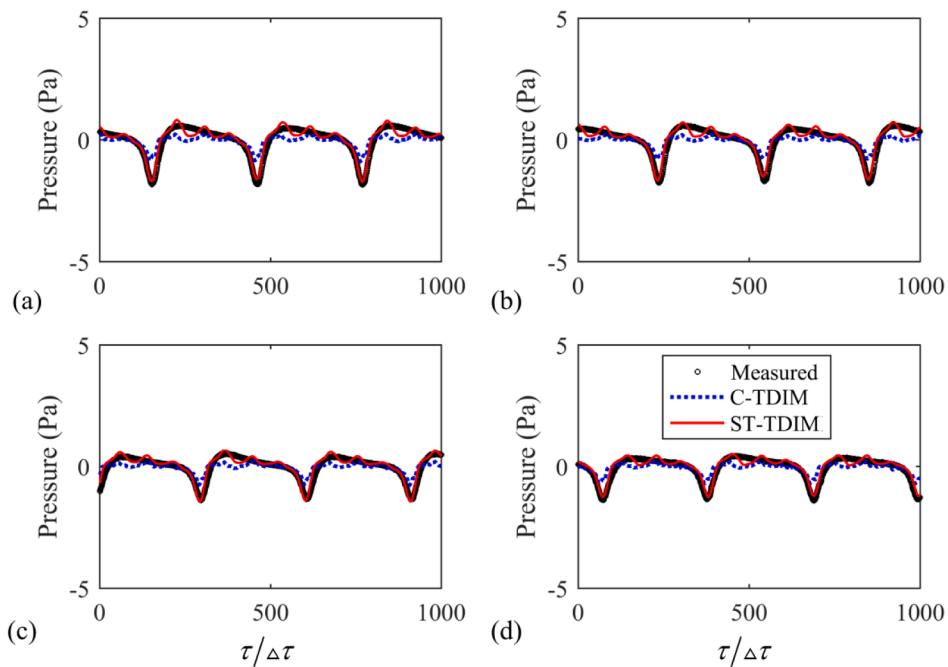

Fig. 15. Comparison of the predicted and measured pressures at four prediction points: (a) M1 (0.2, 0, 0.02) m; (b) M2 (0, 0.2, 0.02) m; (c) M3 (-0.2, 0, 0.02) m; (d) M4 (0, −0.2, 0.02) m.

Fig. 16. The localization results of the two rotating blades (a) by the C-TDIM at time step τ_{460}; (b) by the C-TDIM at time step τ_{615}; (c) by the ST-TDIM at time step τ_{460}; (d) by the ST-TDIM at time step τ_{615}, F indicates the total force.

Fig. 17. Comparison of the reconstructed and reference strength components in the three directions on the tip of two rotating blades: (a) the x_1 direction components of F_a; (b) the x_2 direction components of F_a; (c) the x_3 direction components of F_a; (d) the x_1 direction components of F_b; (e) the x_2 direction components of F_b; (f) the x_3 direction components of F_b.

Fig. 18. Comparison of the predicted and measured pressures at four prediction points: (a) M1 (0.2, 0, 0.02) m; (b) M2 (0, 0.2, 0.02) m; (c) M3 (-0.2, 0, 0.02) m; (d) M4 (0, −0.2, 0.02) m.

advantage of a prior knowledge of the spatial and temporal characteristics of the rotating forces and is well suited to tackle both spatial localization and temporal reconstruction problems simultaneously. Compared to the conventional methods, the proposed one preserves high reconstruction accuracy in undersampling conditions, when a reduced number of input signals are used, thus reducing the measurement and computation cost of the inversion. The method has been initially validated using synthetic noise signals and then validated using measured rotor noise signals. The results of the two validation tests are consistent and confirm the higher accuracy and robustness of the proposed method. Future studies will be carried out to apply the method to real-time source characterization and control.

In addition, it should be pointed out that although the proposed method has no strict limit on the length of the measured data theoretically, it will affect the calculation time. For example, it takes about 5 s to reconstruct the force signals when sound pressure data containing 20 time steps is used. And, as the number of time steps increases, the required calculation time will increase. Therefore, when a long period of sound pressure data needs to be processed, it can be divided into multiple time periods for parallel processing, thus reducing the calculation time.

CRediT authorship contribution statement

Ying Xu: Methodology, Validation, Formal analysis, Investigation. **Xiao-Zheng Zhang:** Conceptualization, Methodology, Software, Writing – original draft. **Damiano Casalino:** Conceptualization, Methodology, Writing – review & editing. **Chuan-Xing Bi:** Supervision, Conceptualization, Methodology, Writing – review & editing.

Declaration of Competing Interest

The authors declare that they have no known competing financial interests or personal relationships that could have appeared to influence the work reported in this paper.

Data availability

Data will be made available on request.

Acknowledgments

The authors thank the three anonymous reviewers and preliminary editor whose comments helped improve the clarity of this manuscript.

References

[1] J.E. Ffowcs Williams, D.L. Hawkings, Sound generation by turbulence and surfaces in arbitrary motion, Philos. Trans. R. Soc. Lond. A264 (1969) 321–342, https://doi.org/10.1098/rsta.1969.0031.

[2] F. Farassat, Linear acoustic formulas for calculation of rotating blade noise, AIAA J. 19 (1981) 1122–113. 10.2514/3.60051.

[3] F. Farassat, G.P. Succi, A review of propeller discrete frequency noise prediction technology with emphasis on two current methods for time domain calculations, J. Sound Vib. 71 (1980) 399–419, https://doi.org/10.1016/0022-460X(80)90422-8.

[4] F. Farassat, G. Succi, The prediction of helicopter discrete frequency noise, Vertica. 7 (1983) 309–320. https://ntrs.nasa.gov/citations/19870001317.

[5] D. Casalino, An advanced time approach for acoustic analogy predictions, J. Sound Vib. 261 (2003) 583–612, https://doi.org/10.1016/S0022-460X(02)00986-0.

[6] F. Avallone, D. Casalino, D. Ragni, Impingement of a propeller-slipstreamon a leading edge with a flow-permeable insert: A computational aeroacoustic study, Int. J. Aeroacoust. 17 (2018) 687–711, https://doi.org/10.1177/1475472X18788961.

[7] G. Romani, D. Casalino, Rotorcraft blade-vortex interac-tion noise prediction using the Lattice- Boltzmann method, Aerosp. Sci. Technol. 88 (2019) 147–157, https://doi.org/10.1016/j.ast.2019.03.029.

[8] G. Romani, E. Grande, F. Avallone, D. Ragni, D. Casalino, Performance and noise prediction of low-reynolds number propellers using the lattice-boltzmann method, Aerosp. Sci. Technol. 125 (2022), 107086, https://doi.org/10.1016/j.ast.2021.107086.

[9] G. Romani, E. Grande, F. Avallone, D. Ragni, D. Casalino, Computational study of flow incidence effects on the aeroacoustics of low blade-tip mach number propellers, Aerosp. Sci. Technol. 120 (2022), 107275, https://doi.org/10.1016/j.ast.2021.107275.

[10] D. Casalino, G. Romani, R. Zhang, H. Chen, Lattice-boltzmann calculations of rotor aeroacoustics in transitional boundary layer regime, Aerosp. Sci. Technol. 130 (2022), 107953, https://doi.org/10.1016/j.ast.2022.107953.

[11] S. Ianniello, The Ffowcs Williams-Hawkings equation for hydroacoustic analysis of rotating blades. Part 1: the rotpole, J. Fluid Mech. 797 (2016) 345–388, https://doi.org/10.1017/jfm.2016.263.

[12] J. Billingsley, R. Kinns, The acoustic telescope, J. Sound Vib. 48 (1976) 485–510, https://doi.org/10.1016/0022-460X(1976)90552-6.

[13] D.H. Johnson, D.E. Dudgeon, Array Signal Processing: Concepts and Techniques, Englewood Cliffs, Prentice Hall, NJ, 1993.

[14] R. Porteous, D.J. Moreau, C.J. Doolan, A review of flow-induced noise from finite wall-mounted cylinders, J. Fluid Struct. 51 (2014) 240–254, https://doi.org/10.1016/j.jfluidstructs.2014.08.012.

[15] R. Merino-Martinez, P. Sijtsma, M. Snellen, A review of acoustic imaging methods using phased microphone arrays, AIAAJ. 10 (2019) 197–230, https://doi.org/10.1007/s13272-019-00383-4.

[16] C. Paolo, M. Milena, C. Paolo, Acoustic beamforming for noise source localization-Reviews, methodology and applications, Mech. Syst. Signal Process. 120 (2019) 422–448, https://doi.org/10.1016/j.ymssp.2018.09.019.

[17] U. Michel, History of acoustic beamforming, in: Proceedings on CD of the 1st Berlin Beamforming Conference, Berlin, 2006. http://www.bebec.eu/Downloads/BeBeC2006/Papers/BeBeC-2006-01 Michel.pdf.

[18] W. Pannert, C. Maier, Rotating beamforming-motion-compensation in the frequency domain and application of high-resolution beamforming algorithms, J. Sound Vib. 333 (2014) 1899–1922, https://doi.org/10.1016/j.jsv.2013.11.031.

[19] K.R. Holland, P.A. Nelson, The application of inverse methods to spatially-distributed acoustic sources, J. Sound Vib. 332 (2013) 5727–5747, https://doi.org/10.1016/j.jsv.2013.06.009.

[20] G. Battista, P. Chiariotti, E. Minnetti, Inverse methods in aeroacoustic three-dimensional volumetric noise source localization and quantification, J. Sound Vib. 473 (2020), 115208, https://doi.org/10.1016/j.jsv.2020.115208.

[21] Y. Liu, A.R. Quayle, A.P. Dowling, P. Sijtsma, Beamforming correction for dipole measurement using two-dimensional microphone arrays, J. Acoust. Soc. Am. 124 (1) (2008) 182–191, https://doi.org/10.1121/1.2931950.

[22] R. Porteous, Z. Prime, C.J. Doolan, D.J. Moreau, V. Valeau, Three-dimensional beamforming of dipolar aeroacoustic sources, J. Sound Vib. 355 (2015) 117–134, https://doi.org/10.1016/j.jsv.2015.06.030.

[23] J.Z. Gao, H.J. Wu, W.K. Jiang, Dipole-based beamforming method for locating dipole sources with unknown orientations in three-dimensional domains, J. Acoust. Soc. Am. 147 (2020) 125–136, https://doi.org/10.1121/10.0000491.

[24] D. Evans, M. Hartmann, J. Delfs, Beamforming for point force surface sources in numerical data, J. Sound Vib. 458 (2019) 303–319, https://doi.org/10.1016/j.jsv.2019.05.030.

[25] B. Christian, I.H. David, B. Martin, Beamforming for directional sources: additional estimator and evaluation of performance under different acoustic scenarios, J. Acoust. Soc. Am. 129 (2011) 2042–2051, https://doi.org/10.1121/1.3557055.

[26] B. Christian, I.H. David, B. Martin, Beamforming with microphone arrays for directional sources, J. Acoust. Soc. Am. 125 (2009) 2098–2104, https://doi.org/10.1121/1.3089221.

[27] X.J. Pan, H.J. Wu, W.K. Jiang, Multipole orthogonal beamforming combined with an inverse method for coexisting multipoles with various radiation patterns, J. Sound Vib. 463 (2019), 114979, https://doi.org/10.1016/j.jsv.2019.114979.

[28] S. Oerlemans, P. Sijtsma, B. Mendez Lopez, Location and quantification of noise sources on a wind turbine, J. Sound Vib. 299 (2007) 869–883, https://doi.org/10.1016/j.jsv.2006.07.032.

[29] W. Ma, H. Bao, C. Zhang, X. Liu, Beamforming of phased microphone array for rotating sound source localization, J. Sound Vib. 467 (2020), 115064, https://doi.org/10.1016/j.jsv.2019.115064.

[30] M.A. Poletti, P.D. Teal, Comparison of methods for calculating the sound field due to a rotating monopole, J. Acoust. Soc. Am. 129 (2011) 3513–3520, https://doi.org/10.1121/1.3589481.

[31] P. Sijtsma, S. Oerlemans, H. Holthusen, Location of rotating sources by phased array measurements, in 7th AIAA/CEAS Aeroacoustics Conference and Exhibit, Maastricht, The Netherlands (2001), https://doi.org/10.2514/6.2001-2167.

[32] X.J. Pan, H.J. Wu, W.K. Jiang, Beamforming correction for the singular problem in identifying rotating sources with non-uniform directivity, J. Acoust. Soc. Am. 147 (2020) 3151–3159, https://doi.org/10.1121/10.0001169.

[33] W.Q. Chen, H.B. Jiang, W.S. He, Dipole source-based virtual three-dimensional imaging for propeller noise, Aerosp. Sci. Technol. 124 (2022) 107562, https://doi.org/10.1016/j.ast.2022.107562.

[34] X.D. Li, S. Zhou, Spatial transformation of the discrete sound field from a propeller, AIAA J. 34 (1996) 1097–1102, https://doi.org/10.2514/3.13198.

[35] J. Luo, X.D. Li, An inverse aeroacoustic problem on rotor wake/stator interaction, J. Sound Vib. 254 (2002) 219–229, https://doi.org/10.1006/jsvi.2001.3671.

[36] A. Gérard, A. Berry, P. Masson, Control of tonal noise from subsonic axial fan. Part 1: Reconstruction of aeroacoustic sources from far-field sound pressure, J. Sound Vib. 288 (2005) 1049–75. 10.1016/j.jsv.2005.01.023.

[37] A. Gérard, A. Berry, P. Masson, Control of tonal noise from subsonic axial fan. Part 2: Active control simulations and experiments in free field, J. Sound Vib. 288 (2005) 1077–1104. 10.1016/j.jsv.2005.01.022.

[38] H. Trabelsi, M. Abid, M. Taktak, T. Fakhfakh, M. Haddar, Reconstruction of the unsteady rotating forces of fan's blade from far-field sound pressure, Appl. Acoust. 86 (2014) 126–137, https://doi.org/10.1016/j.apacoust.2014.03.008.

[39] X.Z. Zhang, C.X. Bi, Y.B. Zhang, L. Xu, A time-domain inverse technique for the localization and quantification of rotating sound sources, Mech. Syst. Signal Process. 90 (2017) 15–29, https://doi.org/10.1016/j.ymssp.2016.12.003.

[40] X.Z. Zhang, C.X. Bi, Y.B. Zhang, L. Xu, On the stability of transient nearfield acoustic holography based on the time domain equivalent source method, J. Acoust. Soc. Am. 146 (2019) 1335–1349, https://doi.org/10.1121/1.5123168.

[41] S. Lee, K.S. Brentner, P.J. Morris, Acoustic scattering in the time domain using an equivalent source method, AIAAJ. 48 (2010) 2772–2780, https://doi.org/10.2514/1.45132.

[42] S. Lee, K.S. Brentner, P.J. Morris, Assessment of time-domain equivalent source method for acoustic scattering, AIAAJ. 49 (2011) 1897–1906, https://doi.org/10.2514/1.J050736.

[43] C.X. Bi, Y. Xu, Y.B. Zhang, X.Z. Zhang, A time-domain inverse method for the localization and quantification of unsteady rotating loading sources, J. Sound Vib. 512 (2021), 116405, https://doi.org/10.1016/j.jsv.2021.116405.

[44] C.X. Bi, L. Hu, Y.B. Zhang, X.Z. Zhang, Reconstruction of the force applied to a plate in the time domain from sound pressure measurements, J. Vib. Acoust. 142 (2020), 031007, https://doi.org/10.1115/1.4046176.

[45] E. Jacquelin, A. Bennani, P. Hamelin, Force reconstruction: analysis and regularization of a deconvolution, J. Sound Vib. 265 (2003) 81–107, https://doi.org/10.1016/S0022-460X(02)01441-4.

[46] Y.M. Mao, X.L. Guo, Y. Zhao, Experimental study of hammer impact identification on a steel cantilever beam, Exp. Techniques 34 (2010) 82–85, https://doi.org/10.1111/J.1747-1567.2009.00530.X.

[47] Z. Li, Z. Feng, F. Chu, A load identification method based on wavelet multi-resolution analysis, J. Sound Vib. 333 (2014) 381–391, https://doi.org/10.1016/j.jsv.2013.09.026.

[48] A. Kazemi Amiri, C. Bucher, Derivation of a new parametric impulse response matrix utilized for nodal wind load identification by response measurement, J. Sound Vib. 344 (2015) 101–113, https://doi.org/10.1016/j.jsv.2014.12.027.

[49] R. Zemcik, J. Bartosek, Z. Lasova, T. Kroupa, Reconstruction of impact on composite airfoil segment using piezoelectric sensors, in: Proceedings of the 7th European Workshop on Structural Health Monitoring, Nantes, France, 2014. https://www.academia.edu/en/67322642.

[50] D. Ginsberg, C.P. Fritzen, New approach for impact detection by finding sparse solution, in: Proceedings of ISMA 2014, Leuven, Belgium, 2014. 10.1109/GLOCOM.2014.7037392.

[51] B. Qiao, X. Zhang, J. Gao, R. Liu, X. Chen, Sparse deconvolution for the large-scale ill-posed inverse problem of impact force reconstruction, Mech. Syst. Signal Process. 83 (2017) 93–115, https://doi.org/10.1016/j.ymssp.2016.05.046.

[52] B. Qiao, X. Zhang, J. Gao, X. Chen, Impact-force sparse reconstruction from highly incomplete and inaccurate measurements, J. Sound Vib. 376 (2016) 72–94.

[53] B. Qiao, X. Zhang, C. Wang, H. Zhang, X. Chen, Sparse regularization for force identification using dictionaries, J. Sound Vib. (2016) 71–86, https://doi.org/10.1016/j.jsv.2016.04.040.

[54] S. Glegg, W. Devenport, Aeroacoustics of Low Mach Number Flows: Fundamentals, Analysis, and Measurement, Academic Press, London, United Kingdom, 2017. 10.1017/aer.2018.128.

[55] C.R. Lowis, P.F. Joseph, Determining the strength of rotating broadband sources in ducts by inverse methods, J. Sound Vib. 295 (2006) 614–632, https://doi.org/10.1016/j.jsv.2006.01.031.

[56] F. Farassat, Derivation of Formulations 1 and 1A of Farassat, NASA, 2007. Technical Report TM 2007-2148 53, https://ntrs.nasa.gov/citations/20070010579.

[57] M. Aucejo, O. De Smet, On a general Iteratively Reweighted algorithm for solving force reconstruction problems, J. Sound Vib. 458 (2019) 376–388, https://doi.org/10.1016/j.jsv.2019.06.041.

[58] M. Aucejo, O. De Smet, A novel algorithm for solving multiplicative mixed-norm regularization problems, Mech. Syst. Signal Process. 144 (2020), 106887, https://doi.org/10.1016/j.ymssp.2020.106887.

[59] L. Hu, C.X. Bi, Y.B. Zhang, X.Z. Zhang, Reconstruction of time-dependent forces acting on a vibrating structure from pressure measurements, J. Acoust. Soc. Am. 150 (2021) 4064–4074, https://doi.org/10.1121/10.0007481.

[60] A. Gramfort, M. Kowalski, M. Hamalainen, Mixed-norm estimates for the m/eeg inverse problem using accelerated gradient methods, Phys. Med. Biol. 57 (2012) 1937–1961, https://doi.org/10.1088/0031-9155/57/7/1937.

[61] M. Aucejo, Structural source identification using a generalized Tikhonov regularization, J. Sound Vib. 333 (2014) 5693–5707, https://doi.org/10.1016/j.jsv.2014.06.027.

[62] M. Aucejo, O. De Smet, Bayesian source identification using local priors, Mech. Syst. Signal Process. 66–67 (2016) 120–136, https://doi.org/10.1016/j.ymssp.2015.05.004.

[63] E.G. Williams, Regularization methods for near-field acoustical holography, J. Acoust. Soc. Am. 110 (2001) 1976–1988, https://doi.org/10.1121/1.1404381.

[64] P.C. Hansen, D.P.O. Leary, The use of the L-curve in the regularization of discrete ill-posed problems, SIAM J. Sci. Comput. 14 (1993) 1487–1503, https://doi.org/10.1137/0914086.

[65] S. Paillasseur, J.H. Thomas, J.C. Pascal, Regularization for improving the deconvolution in real-time near-field acoustic holography, J. Acoust. Soc. Am. 129 (2011) 3777–3787, https://doi.org/10.1121/1.3586790.